Nuclear Instruments and Methods in Physics Research A 729 (2013) 707–717

Contents lists available at ScienceDirect

Nuclear Instruments and Methods in Physics Research A

journal homepage: www.elsevier.com/locate/nima

Monte Carlo simulation of the photon-tagger focal-plane electronics at the MAX IV laboratory

L.S. Myers [a,1], G. Feldman [b], K.G. Fissum [c,*], L. Isaksson [f], M.A. Kovash [d], A.M. Nathan [a], R.E. Pywell [e], B. Schröder [f]

[a] University of Illinois at Urbana-Champaign, Urbana-Champaign, IL 61802, USA
[b] The George Washington University, Washington DC 20052, USA
[c] Lund University, SE-221 00 Lund, Sweden
[d] University of Kentucky, Lexington, KY 40506, USA
[e] University of Saskatchewan, Saskatoon, SK, Canada S7N 5E2
[f] MAX IV Laboratory, Lund University, SE-221 00 Lund, Sweden

ARTICLE INFO

Article history:
Received 23 March 2013
Received in revised form
6 August 2013
Accepted 6 August 2013
Available online 19 August 2013

Keywords:
Tagger hodoscope
Electronics simulation
Rate dependencies

ABSTRACT

Rate-dependent effects in the electronics used to instrument the tagger focal plane at the MAX IV Laboratory have been investigated using the novel approach of Monte Carlo simulation. Results are compared to analytical calculations as well as experimental data for both specialized testing and production running to demonstrate a thorough understanding of the behavior of the detector system.

1. Introduction

The MAX IV Laboratory [1] is the Swedish National Electron Accelerator Facility located in Lund, Sweden. The Tagged-Photon Facility (TPF) at the MAX IV Laboratory [2,3] is the beamline at the facility which utilizes the 200 MeV pulse-stretcher mode [4]. Electrons in pulses with widths of about 200 ns are accelerated to energies up to 200 MeV and then injected into the MAX I pulse-stretcher ring (PSR) at a frequency of 10 Hz. The electrons are then slowly extracted over the following 100 ms, before the arrival of the next pulse from the linac, and then transported to the TPF. In this manner, the pulsed electron beam originating in the injector is converted into a continuous, but non-uniform, electron beam with an average current of approximately 20 nA. Understanding rate-dependent effects in the experiment electronics resulting from the time structure in the electron beam required the efforts reported upon in this paper.

The TPF houses two photon-tagging spectrometers inherited from the Saskatchewan Accelerator Laboratory (SAL) in Saskatoon, Canada [5–7]. These devices are used to perform photonuclear experiments via the well-known photon-tagging technique [8] illustrated in Fig. 1. The electron beam passes through a thin metal radiator ($\sim$100 μm Al), and a small portion ($\sim$0.1%) of the incident electron beam is converted into a bremsstrahlung photon beam. Electrons that do not interact are dumped onto a well-shielded Faraday cup which registers the non-interacting electron-beam current. The resulting bremsstrahlung photon beam passes through a collimator to define its size prior to striking the experimental target. Post-bremsstrahlung electrons are momentum-analyzed using one of the magnetic photon-tagging spectrometers together with a 63-counter plastic-scintillator array positioned at the spectrometer focal plane (FP) [2]. A time coincidence between a reaction product from a photon-target interaction and a recoiling electron is a tagged-photon event.

The energy of a tagged photon is determined from the difference between the energy of the incident electron beam and the energy of the post-bremsstrahlung electron detected in the focal plane. The number of electrons striking a given channel in the FP array is a crucial experimental parameter, as it is part of the overall experimental photon-flux normalization. The number of electrons must be corrected for the tagging efficiency [9], which measures the probability that the bremsstrahlung photon in question passes through the beam-defining collimator and is incident upon the experimental target.

The number of electrons counted in a given FP channel must also be corrected for rate-dependent effects. These effects arise due to the fact that the electron beam striking the radiator is not truly continuous, but rather has a periodic structure of varying intensity. These intensity variations are due to the non-uniform

* Corresponding author. Tel.: +46 46 222 9677; fax: +46 46 222 4709.
E-mail address: kevin.fissum@nuclear.lu.se (K.G. Fissum).
[1] Present address: Duke University, Durham, NC 27708, USA.

0168-9002/$ - see front matter © 2013 Elsevier B.V. All rights reserved.
http://dx.doi.org/10.1016/j.nima.2013.08.032

filling of the PSR by the injector and the frequency of the shaker in the PSR which is used to disturb the electrons from the central orbit of the ring lattice in the extraction process. The measure of this intensity variation is the duty factor of the beam [10]. At an operating current of 20 nA, the average rate in a FP channel is approximately 1 MHz; however, the instantaneous rate in the same FP channel can be as high as 4 MHz [11] due to the duty factor. Using this exact tagging spectrometer and FP detector array at such high rates, Hornidge et al. observed substantial rate-dependent effects in deuterium Compton-scattering data measured at SAL [12,13]. In order to determine the necessary rate-dependent corrections, Pywell developed a Monte-Carlo simulation of the tagger setup [14]. This original simulation has been completely overhauled and adapted to the present experimental conditions of the TPF at the MAX IV Laboratory.

In this paper, we present a detailed comparison between both dedicated test data and experimental production data obtained using the TPF and the overhauled Monte Carlo, and we demonstrate a clear understanding of the rate-dependent effects that we have encountered.

2. Rate-dependent effects

The FP detector hodoscope consists of an array of NE110 scintillators arranged in two parallel rows of scintillators. The front row nearest the exit window of the tagger magnet has 31 elements, while the back row has 32 elements. The relative orientation of the two rows may be varied in order to adjust the overlap between the rows from complete (100%) to 50% (the configuration used for this work). By decreasing the overlap, the recoil-electron energy resolution is increased and consequently the photon-energy resolution is also increased (see Fig. 2).

Each counter is instrumented with a Hammamatsu R1450 photomultiplier tube with a 19 mm head, and high voltage is supplied by a LeCroy 1440 power supply. The signals from the FP counters are passed to LRS 4413 leading-edge discriminators operated in burst-guard mode. These discriminators are used to generate logic signals of widths varying from 25 ns to 50 ns depending upon the experiment in question. Coincidences between two overlapping scintillators in the front and back rows are identified in overlap coincidence modules designed and built at SAL – it is these coincidences that define tagger channels. When operated in 50% overlap mode, the length of the hodoscope is 842 mm, and each of the so-defined tagger channels has a physical width of 13 mm. The logical OR of the 62 FP channels is used as a trigger for a recoil-electron event (see Fig. 3). When a recoil-electron trigger occurs in coincidence with a trigger from the experiment detectors, a candidate tagged-photon event is registered.

Two advantages to requiring a coincidence between the front and back rows of scintillators in the FP hodoscope are that the gamma-ray background in the tagger hall is not registered by the tagger, and that the photon-energy resolution may be increased by varying the relative orientation of the two scintillator planes rather than building a new array with smaller scintillators. However, a major disadvantage of requiring a coincidence between the front and back rows of scintillators in the FP hodoscope is the creation of so-called “ghost events” at high rates. The ghosts are an artificial creation of the instrumentation of the focal plane. The scenario leading to a ghost event is illustrated in the top panel of Fig. 4. Two electrons strike next-to-neighboring channels (counters F1 · B1 and F2 · B2) simultaneously which creates the illusion of an electron in the channel in the middle (counters F1 · B2) – the ghost event. The accidental coincidences that result in ghost events depend on the electron rate, the width of the discriminator output pulses, and the resolving time of the coincidence modules. Because these ghosts are formed in the FP electronics, the accidental coincidences are registered in both the scalers and the TDC modules. This results in a partial cancellation of the effect. Understanding the dependence of the ghosts on the input conditions and determining the amount of cancellation requires a Monte Carlo simulation of the tagger setup and electronics.

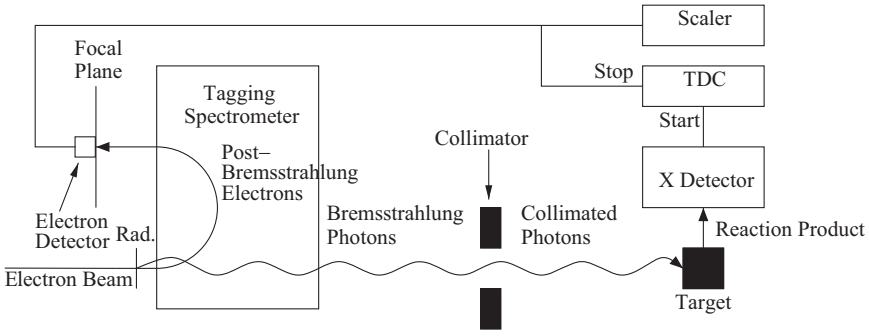

Fig. 1. The photon-tagging technique. Beam electrons may radiate bremsstrahlung photons. Post-bremsstrahlung electrons are momentum analyzed using the photon tagger, which consists of a magnetic tagging spectrometer and a FP array of electron detectors. Bremsstrahlung photons which pass through the collimator strike the experiment target and may induce photonuclear reactions which result in a reaction product being detected. The coincidence between a reaction product and a post-bremsstrahlung electron is a tagged-photon event.

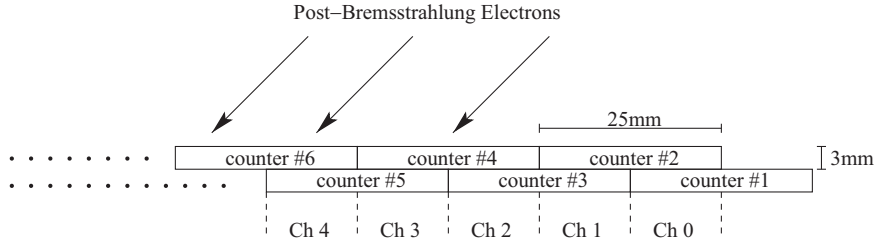

Fig. 2. The FP hodoscope in 50%-overlap configuration. A coincidence between a counter in the front plane (even) and a counter in the back plane (odd) defines a tagger channel. There are a total of 63 counters and 62 channels in the focal plane.

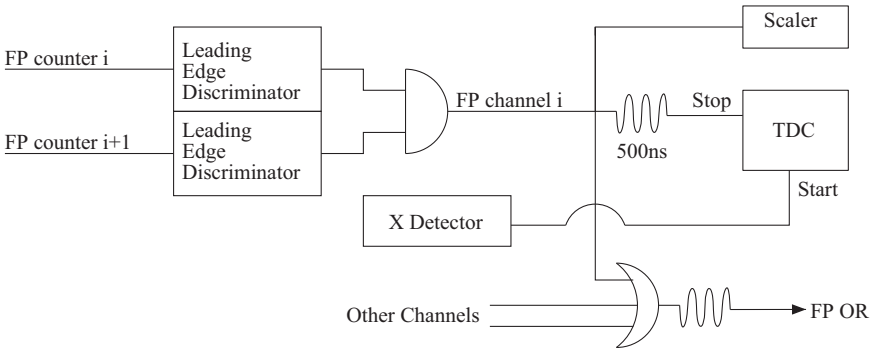

Fig. 3. The FP electronics. A coincidence between an electron-detector signal in the front plane and an electron-detector signal in the back plane defines a tagger channel. The coincidence module looking for these overlaps was from SAL. This signal is counted and used to stop a TDC started by the photonuclear reaction-product detector. The logical OR of all the focal-plane channel signals is the FP OR trigger.

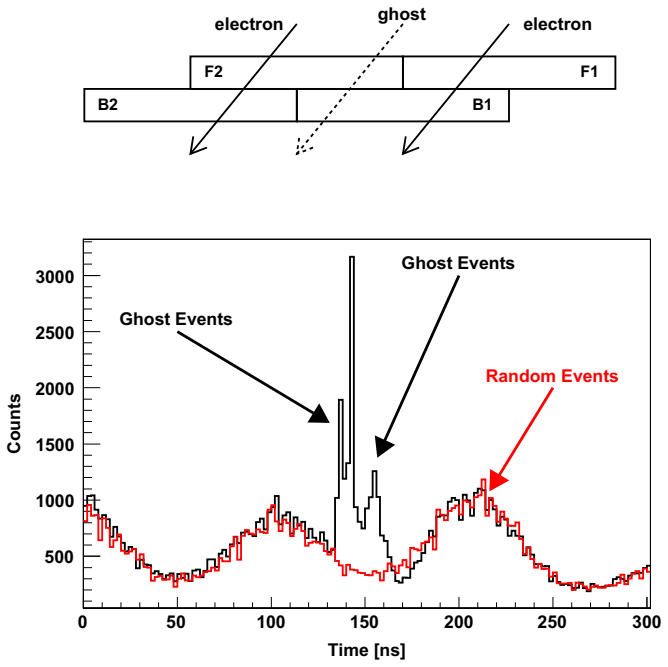

Fig. 4. (Top) The scenario that leads to a ghost event. Real electrons (solid arrows) in next-neighboring FP channels arrive nearly simultaneously. This creates the illusion – or "ghost" – of an electron (dashed arrows) in the counters that constitute the intermediate FP channel. (Bottom) A demonstration of ghost events within the data. A coincidence between the experiment trigger and FP channel 36 has been required. Adjacent FP channel 37 (black) and physically distant FP channel 40 (red) TDC spectra are shown. Both were started by the same experiment trigger. The red spectrum is thus due to untagged, accidental events. The "ripple" in the accidental distribution is discussed in Section 4.2. The black spectrum also shows these untagged, accidental events. In addition, there are three clear peaks between 130 and 170 ns. The sharp, dominant peak is a combination of accidental coincidences and ghosts. The secondary and tertiary peaks to the left and the right are due to ghost events. The multiple peaks were determined to arise from the pulse-timing characteristics of the TDC (see Section 4.1). (For interpretation of the references to color in this figure caption, the reader is referred to the web version of this article.)

High recoil-electron rates can also lead to real electron stops being missed by the leading-edge discriminators (even though they are operated in burst-guard mode) and the overlap coincidence modules due to dead-time effects. They also result in asymmetries in the data acquisition, since the scalers counting the electron signals which are used to normalize the data are much faster than the TDCs which identify tagged-photon events – see Section 4.1. And finally, when single-hit TDCs are employed, a random electron may be detected in the FP channel before the actual electron that corresponds to the tagged photon. The result is

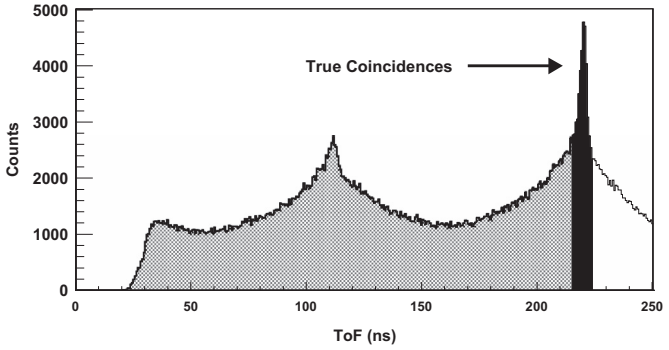

Fig. 5. An illustration of the stolen-coincidence effect in a single-hit TDC spectrum acquired at a high post-bremsstrahlung electron rate. The black peak at channel 225 represents true coincidences between the reaction-product detector and the hodoscope. This point in time is the earliest possible that a true coincidence may be registered. Events in the gray shaded region correspond to random post-bremsstrahlung electrons stopping the FP TDCs before this earliest possible point in time. The true coincidence is thus stolen when a single-hit TDC is used. Note that the "peak" at channel 110 is due to the non-uniform filling of the ring in the extracted electron beam.

that the single-hit TDC stops too early, leading to a well-studied phenomenon known as stolen coincidences [15] – see Fig. 5.

In order to measure the number of stolen coincidences in the data set, a prescaled FP (pFP) trigger is routinely included in the data stream – see Fig. 6. To form this trigger, a representative logic signal from a single FP channel is passed to a bank of three scalers (uninhibited, bad-beam inhibited,[2] and bad-beam OR busy DAQ inhibited). A fourth copy of this signal is bad-beam inhibited, rate-divided (typically by a factor of 10^5), and used as the pFP trigger. It is trickled into the data stream at a rate of $\sim$10 Hz as a valid trigger and is used to start the FP TDCs. As a result, for the pFP-triggered subset of events, the FP TDCs are started by the pFP signal and stopped by the usual recoil-electron signal (recall Fig. 3). Note that the coincidence between the normal recoil-electron signals in the front and back scintillator planes was established using SAL modules, while the same coincidence for the pFP trigger was established using a LRS 622.

Fig. 7 shows a typical TDC spectrum where the start signals were provided by the pFP trigger and the stop signals were provided by recoil electrons striking the focal plane. In the TDC spectrum, we expected to see a single self-timing peak (shown here from channels 165 to 175) and a grouping of events to the left of the self-timing peak (shown here below channel 150) corresponding to stolen coincidences. The appearances of a satellite

[2] Bad beam is defined as the first 1 ms of the extracted beam from the PSR.

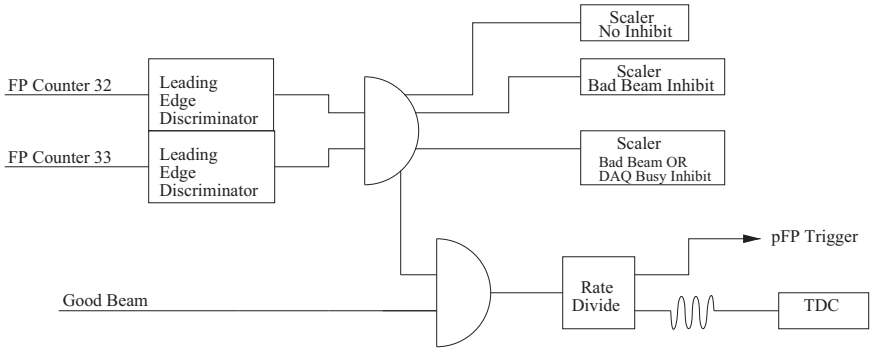

Fig. 6. The pFP trigger. The signal from a single FP channel is rate divided to ~10 Hz and then passed to the DAQ as a valid event trigger and used to start the FP TDCs.

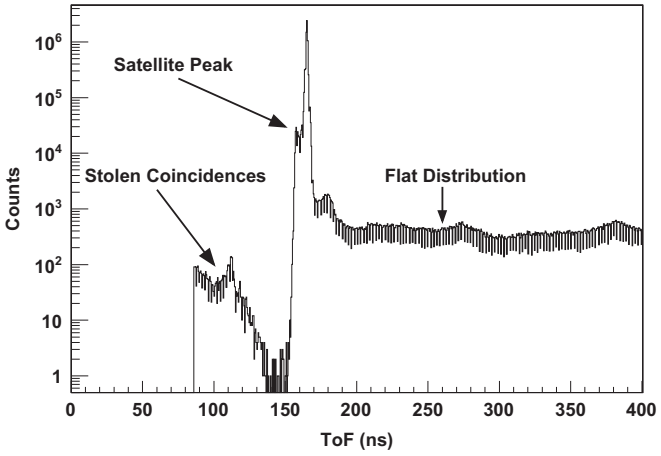

Fig. 7. A typical pFP TDC spectrum. A self-timing peak between channels 165 and 175 is clearly evident. The grouping of events below channel 150 are stolen coincidences – see text for details. The satellite peak between channels 150 and 165 as well as the flat distribution of events from channels 180 to 400 and higher could not be explained without the help of the simulation.

peak (shown here from channels 150 to 165) as well as a flat distribution of events at times greater than the self-timing peak (events ranging from channel 180 to 400 and higher) were a mystery prior to the simulation efforts.

3. Basic features of the simulation

Using the procedure established by Pywell, the Monte Carlo simulation models the FP electronics in 1 ns steps from the recoil-electron detectors to the scalers and TDCs, traversing all of the intermediate electronics in the process. In contrast to the Pywell procedure, our simulation addresses all 62 FP channels simultaneously. In an effort to make the simulation as versatile as possible, it was written so that many of the initial conditions are input from separate files rather than being hard-coded. During each ns of the simulation, the FP channels are checked to see if a recoil electron struck the channel. The probability for such an electron event is dependent on the instantaneous electron rate in the FP channel, which in turn depends on the time structure of the electron beam. Both these parameters are adjustable inputs.

A Poisson distribution is used to generate recoil electrons in the FP channels.[3] If an electron is observed in a given channel, the corresponding counter discriminators are updated, and then the counter discriminator pulses are tracked to the overlap coincidence modules which are updated. The signals from the overlap coincidence modules are then propagated to the FP scalers and TDCs which record the electron. For each recoil electron in a FP channel, there is also a probability that the corresponding photon generates a start for the FP TDCs. The likelihood of this occurring (which is related to the tagging efficiency) is another input to the simulation. Additionally, untagged photons and cosmic-ray events can also be used to start the FP TDCs.[4] If there is an experiment trigger (either a pFP electron, a tagged or untagged photon, or a cosmic ray), the FP TDCs are started and the FP scalers are inhibited. The duration of the inhibit may be adjusted to precisely match the experimental running conditions. Finally, the simulation checks each coincidence in the coincidence modules to see if a corresponding real electron is responsible for generating the coincidence. If no electron was present, then a flag is set which identifies the coincidence output as a ghost event. This flag allows for the analysis of both real and ghost events and leads to the subsequent correction factors for the data.

The original code developed at SAL by Pywell was written in FORTRAN. The new simulation was updated to C++ and was compiled with `gcc`, and the simulation output is written to a ROOT file [17]. The compiled code is run on a 2.66 GHz CPU which takes approximately one hour to simulate the FP electronics for events spanning a time interval of one second. A flow chart describing the simulation is shown in Fig. 8, and a summary of input parameters is presented in Table 1. Most of the inputs to the simulation listed in Table 1 are taken directly from the electronics setup (such as pulse widths) or from the data itself (such as electron rates and tagging efficiency).

4. Input parameters

4.1. Electronics

Once the framework of the tagger simulation was developed, it was necessary to understand the response of the various electronics modules in order to implement them correctly. This required a thorough understanding of the leading-edge discriminators, various coincidence modules, TDCs, and scalers.

As previously mentioned, the LRS 4413 leading-edge discriminators used to instrument the focal plane were operated in burst-guard mode, which resulted in behavior that was especially important at high rates. The modules are designed to produce an output pulse of a fixed, user-determined width when the threshold is crossed. If a second event arrives at the discriminator before the end of the previous output pulse, the output will be updated and will extend to the greater of the fixed width or the threshold

[3] The individual FP counter rates were not recorded.

[4] The corresponding count rate is used to generate a random event using a Poisson distribution.

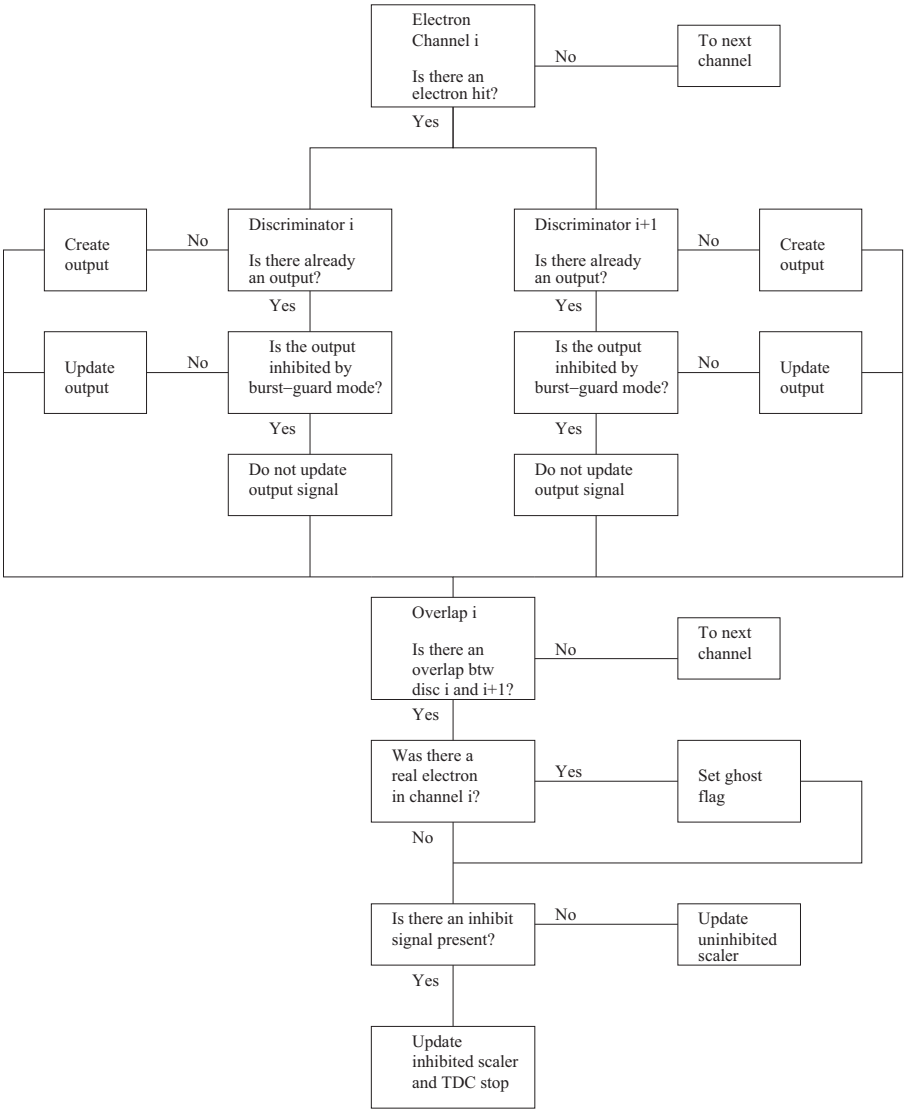

Fig. 8. Flowchart describing the simulation. See text for details.

Table 1
Simulation input parameters. See text for details.

Input parameter	Description
Total run time	Number of ns to run the simulation
Electron rate in reference channel	Taken from data, ~ 1 MHz
Cosmic-ray event rate	Taken from data, ~ 50 Hz
Untagged event rate	Taken from data, ~ 50–150 Hz
Probability of a tagged event	Taken from data, $\sim 50\%$ (inbeam), $\sim 0.5\%$ (scattering)
Electron rate relative to reference channel	Taken from data, ~ 1–4
Focal-plane discriminator pulse width	Leading edge, ~ 25–50 ns
Inhibit duration	Bad beam or DAQ busy, $\sim 1,$ ms
Geometric double	Recoil electron strikes adjacent channels, $\sim 1\%$
pFP trigger channel	Channel 32
pFP trigger pulse width	Same as focal-plane discriminator pulse width, ~ 25–50 ns
pFP overlap properties	Flag, module (non)updating
pFP trigger	Flag, on/off
Duty-factor meter (DFM) counters	Counter 20 and counter 50
DFM pulse widths	~ 25–50 ns
DFM overlap characteristics	Flag, module (non)updating
Prompt-peak location	Δt between FP TDC start and prompt peak, ~ 100 ns
Periodicity of the electron-beam profile	Long enough to generate several repetitions
Electron-beam profile	See top panel of Fig. 12

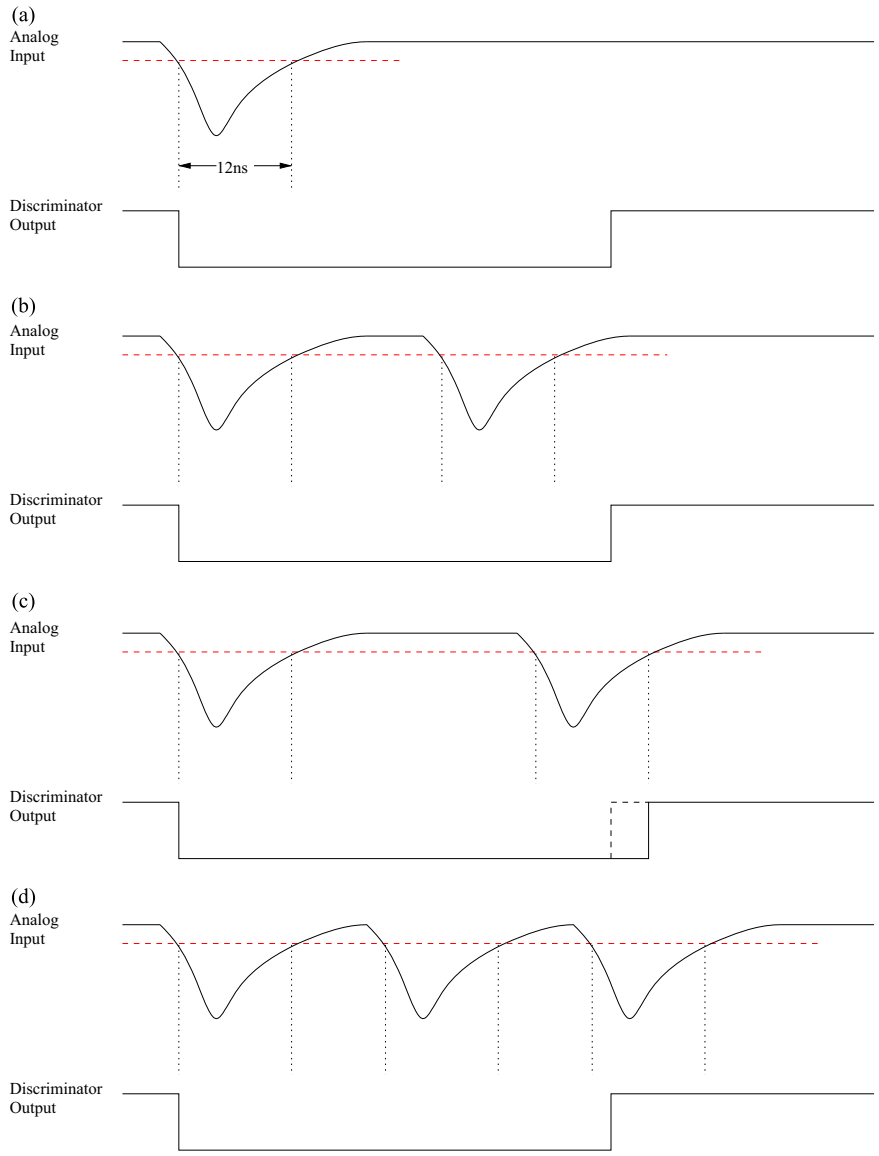

Fig. 9. An illustration of the behavior of the LRS 4413 leading-edge discriminators operating in burst-guard mode. See text for details.

re-crossing of the second input pulse. Any subsequent inputs will be ignored until the fixed width has passed and the discriminator is reset.

Fig. 9 illustrates the burst-guard behavior of the LRS 4413 leading-edge discriminator. In panel (a), a single analog signal corresponding to an electron is discriminated, resulting in a 40 ns output pulse. Panels (b) and (c) show the conditions for updating the output pulse with a second electron. In panel (b), the re-crossing associated with the second electron occurs before the original output ends – the output pulse is thus the same as in panel (a), and the second electron is missed. In panel (c), the second re-crossing occurs after the output would have ended, so the duration of the output signal is extended. Third hits are never registered, as shown in panel (d).

The SAL overlap coincidence modules used for forming the pulses that were sent to the FP TDCs and scalers were continuously updating. An output pulse was generated whenever the two input pulses overlapped and was terminated whenever one or both inputs were reset. An overlap of at least 3 ns was necessary to produce an output pulse. This behavior is asymmetric to the LRS 622 coincidence module used to generate the pFP trigger – it produced a fixed output pulse that began when the discriminator output signals from the two FP counters overlapped. The CAEN V775 single-hit TDCs used to instrument the focal plane were experimentally determined to require input pulses of at least 11 ns in width in order to register the pulses. In contrast, the CAEN 830 scalers which counted the recoiling electrons were experimentally determined to require input pulses of at least 3 ns in width in order to register the pulses.[5]

Fig. 10 shows the count rate relative to the trigger rate for FP channel 24 for a wide range of relative pulse timings generated by a pulser. In this test, pulser triggers running at 10 Hz were fed into the SAL overlap coincidence unit inputs for the front and back scintillator planes corresponding to FP channel 24. Tests were performed for pulse widths of 25 ns, 35 ns, and 45 ns. The relative timing between the front and back pulses was then varied in steps of a few ns over a total range of ± 40 ns. The open circles correspond to the FP channel 24 scaler, while the filled triangles correspond to the FP channel 24 TDC. Clearly, over the entire

[5] Note that this ~ 3 ns width is comparable to the smallest pulse that can be generated by the coincidence modules, so that the scalers may register even shorter pulses.

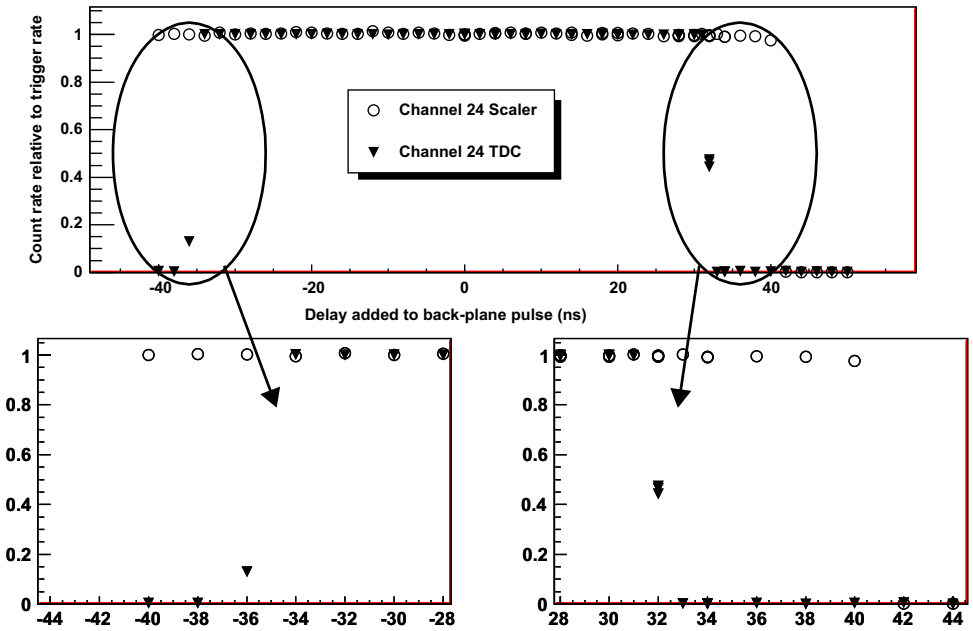

Fig. 10. A comparison of the response of FP channel 24 TDCs and scalers when the pulses from the front-scintillator plane and the back-scintillator plane are set to 45 ns in width and the relative timing of the back-plane pulses is then varied by ± 40 ns. Open circles correspond to the scaler and filled triangles correspond to the TDC. The bottom left panel is an enlargement of the top panel from -44 ns to -28 ns and the bottom right panel is an enlargement of the top panel from 28 ns to 44 ns. There is a clear asymmetry in the response of the two modules for shifts in relative timings of more than 30 ns.

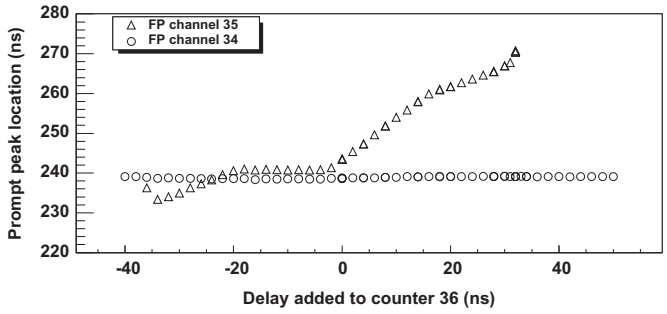

Fig. 11. Ghost timing. Recall Fig. 4. The location of the overlap coincidence peak in the FP TDCs for channels 34 and 35 is shown as a function of varying the delay in FP counter 36. See text for details.

dynamic range investigated, the CAEN V830 scalers were able to register the signals from the SAL overlap coincidence units. This was true even when the timing of the back-plane pulse relative to the front-plane pulse was artificially fixed 40,ns early or 40 ns late, resulting in an overlap pulse of ~ 3 ns width. On the other hand, the CAEN V775 single-hit TDCs only registered pulses when the timing of the back-plane pulse relative to the front-plane pulse was between 35 ns early and 30 ns late, resulting in an overlap pulse of ~ 11 ns width.

The fact that a ~ 3 ns overlap pulse could generate a pFP trigger and, consequently, a start signal for the FP TDCs but an ~ 11 ns overlap pulse was needed to generate a stop signal resulted in missing stops. The flat distribution from channels 180 to 400 in Fig. 7 thus resulted from random electrons stopping the FP TDC. Obviously, this important asymmetry in the response of the electronics must be taken into account and corrected in order to properly normalize experimental data.

A peculiar feature of the FP TDCs and/or overlap coincidence modules was observed during the test of the FP TDC resolving time. This test was performed using a 10 kHz pulser, and the signal from the pulser was split into three identical copies, which were then passed to the electronics connected to FP counters 34 (front plane), 35 (back plane), and 36 (front plane). Holding the timing fixed for the counters 34 and 35 electronics, it was observed that as delay was added to or removed from counter 36, the location of the counter 35/36 (channel 34) overlaps coincidence peak in the FP TDC varied by as much as 40 ns. A shift was expected to some degree (for example, for fixed counters 34 and 35, as counter 36 is mistimed to arrive later and later, then the coincidence peak representing counter 35/36 overlaps should also shift in time by the amount of the mistiming); however, the behavior shown in Fig. 11 is not consistent with this behavior. There is a shift in the prompt peak location at around -30 ns of added delay as well as non-linear behavior (a "kink" and then a "dogleg") above $+20$ ns. This variation in the location of the coincidence peak as a function of the relative timing of the front-plane and back-plane signals explains the ghost-peak structure in Fig. 4 (recall the three peaks) and the satellite peak between channels 150 and 165 in Fig. 7. This effect was included in the simulation.

4.2. Electron-beam profile

One very important input parameter to the simulation is the time profile of the electron beam extracted from the PSR. Unfortunately, this is not directly accessible from the data. To obtain the time profile of the electron beam, the subset of the data pertaining only to pFP triggers was employed. This data set was generated by requiring a recoil-electron signal in a specific FP channel. For this data set, recoil electrons striking FP channels well-separated from the selected channel were taken to be accidentals. The FP TDC distributions for these distant channels were then summed together to produce a purely accidental FP TDC spectrum, $A(t)$, with high statistics. This spectrum was then related to the true electron-beam profile via an auto-correlation function according to

$$A(t) = \int_{-\infty}^{\infty} P(T)P(t+T)\,dT. \quad (1)$$

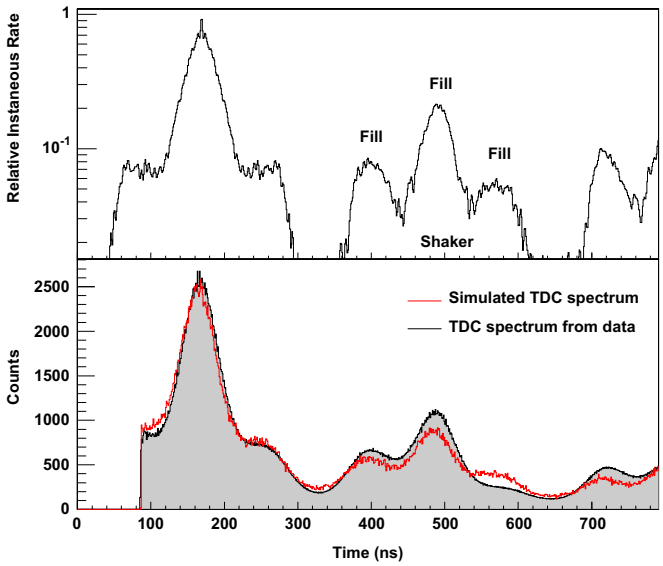

Fig. 12. (Top panel) The electron-beam time profile, $P(t)$. The observed time structure is due to incomplete filling of the 32.4 m diameter (108 ns) MAX I PSR and the 3.3 MHz frequency (305 ns period) of the extraction shaker. The dropoff between the intensity of the first pulse and the second pulse is roughly a factor of four. This dropoff rapidly vanishes after the second pulse. The profile repeats throughout the 100 ms extraction of the beam. See text for details. (Bottom panel) A comparison between a simulated accidental TDC spectrum, $A(t)$, for the OR of all 62 FP TDCs and data (shaded). The simulation input was the electron-beam profile shown in the top panel together with the parameters presented in Table 1. Agreement is excellent, confirming our understanding of the input parameters. (For interpretation of the references to color in this figure caption, the reader is referred to the web version of this article.)

The method of Fourier transform was then used to extract the beam profile $P(t)$ shown in the top panel of Fig. 12.[6] The secondary and tertiary time structures in this distribution result from the 3.3 MHz frequency (305 ns period) of the shaker used in the extraction of the electron beam and the incomplete filling of the 32.4 m diameter (108 ns period) MAX I PSR.

4.3. Instantaneous electron beam rates

The determination of the average instantaneous beam rate over one beam period (hereafter, the instantaneous rate) is crucial for an accurate calculation of both the stolen coincidences and the ghost corrections. The rate is given by the time constant of the accidental TDC spectrum which can be determined by fitting the data with an exponential function. However, due to the complicated time structure of the beam, the method of extracting the rate must be carefully chosen so as not to be sensitive to the fitting region selected. This is done by defining the fitting function as

$$f(t) = p_0 A(t) e^{-Rt} + p_1 e^{(t-t_0)^2/2\sigma^2}, \quad (2)$$

where p_0 and p_1 are constants, $A(t)$ is the FP TDC spectrum for accidental events (see Eq. (1)), and R is the instantaneous rate. Since the spectrum also contains some true coincidences, a Gaussian function centered at t_0 is used to account for these events so as to eliminate any bias they might cause in the fitting procedure. As seen in Fig. 13, this method accurately fits the data.

[6] An array was created representing the accidental spectrum with one entry per ns. The FFT transform function in ROOT was then used to produce $P^2(T)$. High-frequency terms deemed unimportant were filtered before taking the square root of $P^2(T)$ and performing the inverse FFT.

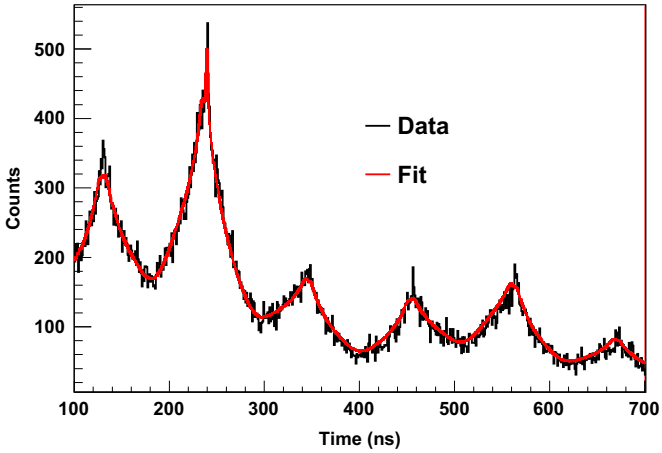

Fig. 13. The result of fitting Eq. (2) to FP channel 17 TDC data (shown as a histogram). The time constant of the fit is employed in the simulation as the instantaneous electron rate. The true coincidences occur at t_0=240 ns.

5. Comparison to data

5.1. Focal-plane TDC spectrum

Fig. 12 (bottom panel) shows a comparison between the simulated FP TDC spectrum for accidentals for the OR of all 62 FP TDCs and data. The inputs included the electron-beam profile shown in the top panel of Fig. 12 together with all the parameters presented in Table 1. A correction based on the location of the coincidence peak has been applied to align all of the individual 62 FP TDC spectra. The broad peaks in this spectrum are due to the structures in the electron beam extracted from the PSR. Time periods when greater numbers of electrons are extracted from the PSR correspond to enhancements in the number of tagged photons available to the experiment. The agreement between the data and the simulation is excellent.

5.2. Scaler rates and system deadtime

A rate-dependent study of the effects of deadtime in the FP electronics was performed using a standard 45% duty-factor electron beam to determine the impact on the FP scalers. FP channels 5, 15, 25, and 35 were first tested individually, then OR-ed together in two groups of two (5 and 15, 25 and 35), and finally tested as a single group of four in order to conveniently increase the available rates. The counts in the individual channels were used to determine the actual numbers of counts reaching the FP scalers. The fraction of counts reaching the FP scalers for the twofold and fourfold ORs was then monitored as a function of rate. Fig. 14 shows data (solid circles) for the fraction of expected counts in the twofold and fourfold configurations as a function of average recoil-electron rate. Simulated values are shown for a duty factor of about 50% (open circles). The inset shows the densely populated region from 0 to 1 MHz. Clearly, the simulation does an excellent job of predicting the loss of counts in the FP scalers due to deadtime effects.

5.3. Prescaled focal-plane trigger

It is straightforward to compare the data collected using the pFP trigger to the simulation because the trigger source is one of the FP channels. The number of stolen coincidences in the pFP trigger channel is the ratio of the number of counts in the TDC prompt peak (recall Fig. 7) to the total number of triggers. Since events with an output width of less than 11 ns in the coincidence

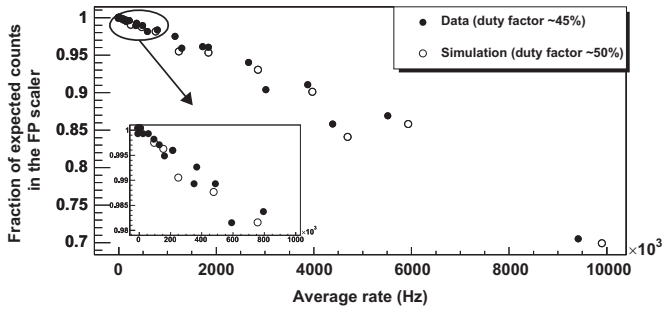

Fig. 14. Recoil-electron loss effects. A comparison between data (filled circles) and simulation (open symbols) of the fraction of post-bremsstrahlung electrons counted by the FP scalers as a function of average recoil-electron rate. The inset expands the region up to 1 MHz. See text for details.

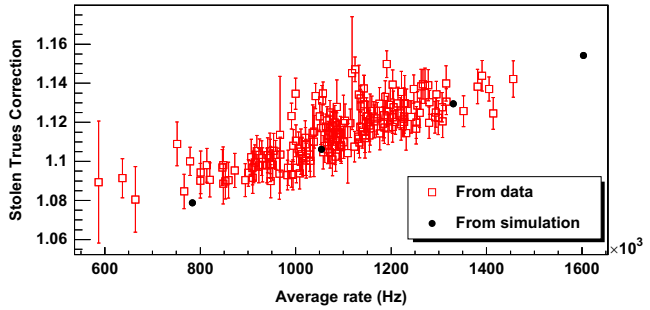

Fig. 15. A comparison between the stolen-coincidences corrections for the pFP trigger obtained from the data (open squares) and the simulation (filled circles).

overlap module do not register a stop in the FP TDCs, it is important to include events to the right of the prompt peak as stolen coincidences since these events were not recorded due to the limitations in the electronics setup. Using data, the stolen coincidences can be determined for the pFP trigger on a run-by-run basis (recall Fig. 7). The stolen coincidences can also be calculated using the simulation at several recoil-electron rates. A comparison of the two approaches is presented in Fig. 15.

5.4. Stolen-coincidence correction

A method for analytically calculating the stolen coincidences for a nearly continuous beam is given in Ref. [15]. The stolen-coincidence correction is given by

$$f_{\text{stolen}} = e^{R\tau} \tag{3}$$

where R is the electron rate and τ is the time between the start of the TDC and the arrival of the corresponding tagged electrons. The stolen-coincidence correction can also be determined via the simulation. The simulated, tagged-photon TDC spectrum (see Fig. 16) shows both prompt events and stolen coincidences. The fraction of stolen coincidences determined using the simulated tagged photons is given by

$$f_{\text{stolen}}^{\text{sim,tag}} = \frac{N}{N_{\text{prompt}}} \tag{4}$$

where N is the total number of events and N_{prompt} is the number of events arriving during the prompt window.

Several values of R and τ were chosen as simulation inputs in order to compare the simulated stolen coincidences to those predicted by Eq. (3). The results are shown in Table 2. Agreement is excellent.

Another method [16] for determining the stolen-coincidence correction determines the correction from the accidental FP TDC spectrum [16] (see Fig. 16). With this approach, the correction

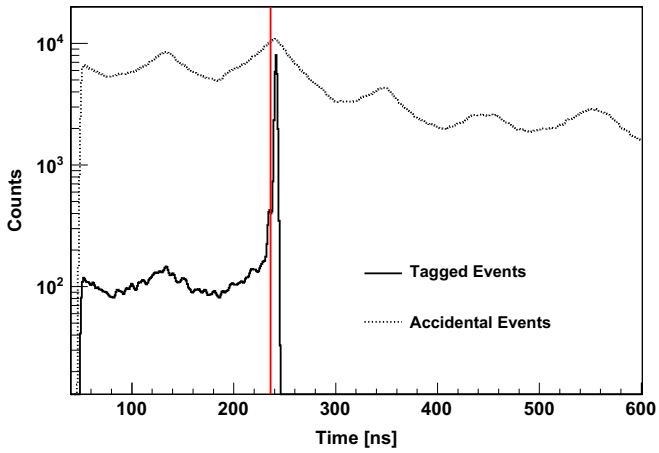

Fig. 16. Spectra for FP channel 30 used to obtain the stolen-coincidence correction via Eq. (5). The lower solid spectrum corresponds to the tagged-photon TDC, while the upper dotted spectrum is simulated accidentals. The prompt peak is located at t_0=240 ns. Stolen coincidences appear to the left of this peak. The red line indicates the location of t_{left}. See text for details. (For interpretation of the references to color in this figure caption, the reader is referred to the web version of this article.)

Table 2
Comparison of the fraction of stolen coincidences obtained using Eq. (3) and the simulation.

$\text{Rate}_{\text{inst}}$ (MHz)	τ (ns)	$f_{\text{stolen}}^{\text{calculated}}$	$f_{\text{stolen}}^{\text{simulated}}$
1.0	19	1.019	1.018 ± 0.001
2.0	19	1.039	1.036 ± 0.001
1.0	199	1.220	1.211 ± 0.001
2.0	199	1.489	1.477 ± 0.002

Table 3
Comparison of the of the stolen-coincidence correction obtained using Eq. (5) applied to the accidental TDC spectrum and Eq. (4) applied to the tagged photons TDC spectrum.

FP ch	$f_{\text{stolen}}^{\text{accidentals}}$	$f_{\text{stolen}}^{\text{tagged}}$
0	1.521	1.519
10	1.567	1.578
20	1.672	1.670
30	1.739	1.738
40	1.768	1.785
50	1.900	1.916
60	2.029	2.056

factor is given by

$$f_{\text{stolen}}^{\text{accidentals}} = \frac{N}{N - N_{t<t_{\text{left}}}} \tag{5}$$

where N is the total number of events and $N_{t<t_{\text{left}}}$ is the number of events arriving prior to the coincidence peak (located at t_0). The stolen-coincidence correction was calculated for both a simulated accidental FP TDC spectrum and the TDC spectrum of the tagged photons. The results are shown in Table 3. Agreement is excellent.

5.5. Ghosts correction

The correction for the rate-dependent ghost effect differs from the stolen-coincidence correction in that an exact analytical form for the correction does not exist. However, it is possible to compare the results of the simulation to the values used by Hornidge et al. [12,13]. Unfortunately, it is impossible to replicate the exact parameters of the SAL configuration. Additionally, the results given by Hornidge et al. are run-averaged results. Still, a

Table 4
Comparison of the ghost correction obtained in Ref. [12] and our simulation.

$\text{Rate}_{\text{inst}}$ (MHz)	$f_{\text{ghosts}}^{\text{Hornidge}}$	$f_{\text{ghosts}}^{\text{thiswork}}$
1.400	1.019	0.993
4.755	1.076	1.007

comparison of the ghost corrections is useful in evaluating the overall accuracy of our FP simulation.

In order to perform such a comparison, the beam conditions were reconstructed as carefully as possible to best reproduce the conditions of the SAL experiment. The beam rates (1.4 and 4.755 MHz) were chosen to match two of those listed by Hornidge et al. The ghost correction is defined as

$$1/f_{\text{ghost}} = \sigma_M/\sigma \tag{6}$$

where σ_M is the measured cross-section and σ is the real cross-section. The correction factors predicted by the FP simulation are compared to the values obtained by Hornidge et al. in Table 4. The apparent disagreement in these results is likely due to undocumented differences in the two experimental setups (for example: discriminator modes, pulse timing, TDC behavior, and beam structure). It is probably impossible to improve the agreement without completely recreating the precise conditions of the SAL experiment.

5.6. Systematic uncertainties

The systematic uncertainties in the ghosts and stolen-coincidence corrections was determined as a function of variations in (1) the FP discriminator pulse width, (2) the time profile of the stretched electron beam leaving the PSR, and (3) the electron rate in the individual FP channels.

During the inaugural run periods at the TPF, the FP discriminator pulse widths were typically set to (50 ± 1) ns.[7] In the simulation, the discriminator pulse widths were varied by ± 2 ns to see how the corrections were affected. In this case, both the stolen-coincidence and ghosts correction varied by less than 0.5%.

Understanding the effect of the time profile of the beam on the corrections was more involved. Conceptually, the electron-beam profile after the PSR could be more uniform ("flatter" as a function of time representing a more continuous beam) or less uniform (higher peaks and lower valleys as a function of time representing a less continuous beam) than the profile used. To obtain a more uniform time profile, $[P(t)]^{0.75}$ was employed; the less uniform profile was given by $[P(t)]^{1.33}$. Exponents smaller than 0.75 or larger than 1.33 resulted in simulated accidental TDC spectra that did not reproduce the data. The variation in the stolen-coincidence correction due to these extreme profiles was less than 2%. The variation of the ghosts correction was less than 3%.

The stolen-coincidence correction depends on the electron rate according to Eq. (3). Further, a rate-independent method to extract the correction is presented in Eq. (4). The difference between these methods is typically 2% or less. Using Eq. (3) and assuming the electron rate varies by $\sim 10\%$, the correction is found to have a systematic uncertainty of $\leq 5\%$. Combining these results, the variation of the stolen-coincidence correction as a function of electron rate is taken to be 5%. The effect of the electron rate on the ghosts correction was investigated by varying the nominal electron beam rate during the simulation by $\pm 25\%$. The ghost correction varied by less than 1% over this range of beam rates.

[7] Today, the FP discriminator pulse widths are typically set to (25 ± 1) ns.

Table 5
Systematic uncertainties in the stolen-coincidence and ghosts corrections due to simulation parameter variations.

Varied parameter	Effect on correction	
	Stolen coincidences (%)	Ghosts (%)
FP discriminator pulse width	0.5	0.5
Time profile of the extracted electron beam	2	3
Electron rate in FP channels	5 (see text)	1

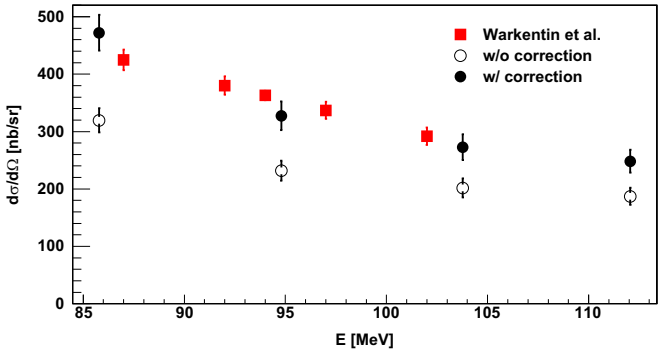

Fig. 17. Absolute differential cross-section data corrected for rate-dependent effects as outlined in this paper compared to published data. Statistical uncertainties only are shown. See text for details.

Table 6
Stolen-coincidence and ghosts corrections applied to the ^{12}C data shown in Fig. 17. Non-negligible statistical uncertainties are listed.

Photon energy (MeV)	86	95	104	112
Uncorrected cross-section (nb/sr)	320 ± 21	232 ± 17	202 ± 16	187 ± 15
Stolen trues correction	1.49	1.43	1.37	1.33
Ghosts correction	0.99	0.99	0.99	1.00
Corrected cross-section (nb/sr)	472 ± 31	327 ± 25	273 ± 22	248 ± 20

A summary of the systematic uncertainties in the stolen-coincidence and ghosts corrections due to simulation parameter variations is presented in Table 5.

5.7. Carbon elastic scattering cross-section for photons

As an illustration of the success of our Monte Carlo method for addressing rate-dependent effects, Fig. 17 presents a comparison between the absolute differential cross-section recently obtained at the TPF at the MAX IV Laboratory and existing data published by Warkentin et al. [18] (filled squares) for elastic photon scattering from ^{12}C at a lab angle of 60° performed at SAL. Error bars reflect statistical uncertainties only. The open circles show our cross-section data prior to correction for rate-dependent effects, while the filled circles show the same data after correction for rate-dependent effects. The agreement between the two data sets is excellent. A summary of the rate-dependent corrections is presented in Table 6.

6. Summary

Rate-dependent effects in the electronics used to instrument the tagger focal plane at the Tagged-Photon Facility at the MAX IV Laboratory have been investigated using a dedicated Monte Carlo simulation. The Monte Carlo simulation incorporates the unique

behaviors of each of the critical focal-plane instrumentation modules. Results have been compared to analytical calculations of these effects, as well as experimental data collected for a series of specialized tests of the rate-dependent response. The simulation agrees very well with both. Further, the output of the simulation has been used to normalize high-rate tagged-photon production data (1 MHz average and up to 4 MHz instantaneous rates per focal-plane channel). Rate-corrected cross-section data are in excellent agreement with previous results obtained at lower instantaneous rates. We assert that this Monte Carlo simulation is of fundamental importance to the analysis of all experimental data from the Tagged-Photon Facility at the MAX IV Laboratory and, in principle, is adaptable to any high-rate coincidence experiment.

Acknowledgements

This project was supported by the US National Science Foundation Grant No. 0855569, as well as The Swedish Research Council, the Crafoord Foundation, and the Royal Physiographic Society in Lund. The authors gratefully acknowledge the Data Management and Software Centre, a Danish Contribution to the European Spallation Source ESS AB, for generously providing access to their computations cluster.

References

[1] ⟨https://www.maxlab.lu.se⟩.
[2] J.-O. Adler, M. Boland, J. Brudvik, K. Fissum, K. Hansen, L. Isaksson, P. Lilja, L.-J. Lindgren, M. Lundin, B. Nilsson, D. Pugachov, A. Sandell, B. Schröder, V. Avdeichikov, P. Golubev, B. Jakobsson, J.R.M. Annand, K. Livingston, R. Igarashi, L. Myers, A. Nathan, W.J. Briscoe, G. Feldman, M. Kovash, D. Branford, K. Föhl, P. Grabmayr, V. Takau, G. O'Rielly, D. Burdeynyi, V. Ganenko, V. Morochovskyi, G. Vashchenko, Nuclear Instruments and Methods in Physics Research Section A 715 (2013) 1.
[3] ⟨https://www.maxlab.lu.se/node/1090⟩.
[4] L.-J. Lindgren, Nuclear Instruments and Methods in Physics Research Section A 492 (2002) 299.
[5] J.M. Vogt, R.E. Pywell, D.M. Skopik, E.L. Hallin, J.C. Bergstrom, H.S. Caplan, K. I. Blomqvist, W. Del Bianco, J.W. Jury, Nuclear Instruments and Methods in Physics Research Section A 324 (1993) 198.
[6] Annual Report 1994, Saskatchewan Accelerator Laboratory, pp. 21–23.
[7] Annual Report 1995, Saskatchewan Accelerator Laboratory, pp. 27–29.
[8] See for example J.-O. Adler, B.-E. Andersson, K.I. Blomqvist, B. Forkman, K. Hansen, L. Isaksson, K. Lindgren, D. Nilsson, A. Sandell, B. Schröder, K. Ziakas, Nuclear Instruments and Methods in Physics Research Section A 294 (1990) 15.
[9] See for example J.-O. Adler, B.-E. Andersson, K.I. Blomqvist, K.G. Fissum, K. Hansen, L. Isaksson, B. Nilsson, D. Nilsson, H. Ruijter, A. Sandell, B. Schröder, D. A. Sims, Nuclear Instruments and Methods in Physics Research Section A 388 (1997) 17.
[10] J.M. Vogt, R. Florizone, Nuclear Instruments and Methods in Physics Research Section A 339 (1994) 425.
[11] L.S. Myers, Ph.D. Thesis, University of Illinois at Urbana-Champaign, USA, 2010, Unpublished; see also ⟨https://www.maxlab.lu.se/sites/default/files/myers.pdf⟩.
[12] D.L. Hornidge, Ph.D. Thesis, University of Saskatchewan, Canada, 1999, Unpublished; see also ⟨http://www.mta.ca/~dhornidg/hornidge_phd.pdf⟩.
[13] D.L. Hornidge, B.J. Warkentin, R. Igarashi, J.C. Bergstrom, E.L. Hallin, N.R. Kolb, R.E. Pywell, D.M. Skopik, J.M. Vogt, Physical Review Letters 84 (2000) 2334.
[14] R.E. Pywell, Subatomic Physics Internal Reports, University of Saskatchewan, Canada, 2009, Unpublished; see also ⟨http://nucleus.usask.ca/technical_reports/other/TaggerSim-1.1.pdf⟩.
[15] R.O. Owens, Nuclear Instruments and Methods in Physics Research Section A 288 (1990) 574.
[16] L. Van Hoorebeke, D. Ryckbosch, C. Van den Abeele, R. Van de Vyver, J. Dias, F. De Smet, B. Schröder, D. Nilsson, Nuclear Instruments and Methods in Physics Research Section A 321 (1992) 230.
[17] ⟨http://root.cern.ch⟩.
[18] B.J. Warkentin, D.L. Hornidge, R. Igarashi, J.C. Bergstrom, E.L. Hallin, N.R. Kolb, R.E. Pywell, D.M. Skopik, J.M. Vogt, G. Feldman, Physical Review C 64 (2001) 014603.